

Wave-mixing cathodoluminescence microscopy of low-frequency excitations

Received: 1 August 2025

Accepted: 26 November 2025

Published online: 22 December 2025

 Check for updatesLeila Prelat¹, Eduardo J. C. Dias^{1,3} & F. Javier García de Abajo^{1,2}✉

Nonlinear optical phenomena such as parametric amplification and frequency conversion are typically driven by external optical fields. Free electrons can also act as electromagnetic sources, offering unmatched spatial precision. Therefore, combining optical and electron-induced fields via the nonlinear response of material structures holds potential for revealing new physical phenomena and enabling disruptive applications. Here, we theoretically investigate wave mixing between external light and the evanescent fields of free electrons, giving rise to inelastic photon scattering mediated by the second-order nonlinear response of a specimen. Specifically, an incident photon may be blue- or red-shifted, while the passing electron correspondingly loses or gains energy. These processes are strongly enhanced when the frequency shift matches an optical resonance of the specimen. We present a general theoretical framework to quantify the photon conversion probability and demonstrate its application by revealing far-infrared vibrational fingerprints of retinal using only visible light. Beyond its fundamental interest, this phenomenon offers a practical approach for spatially mapping low-frequency excitations with nanometer resolution using visible photon energies and existing electron microscopes.

Upon irradiation of a material with sufficiently intense monochromatic light, a polarization is induced that contains harmonics of the incident frequency¹. In addition, when the material is illuminated with polychromatic light, wave-mixed components also appear at the sum and difference of the external optical frequencies. These nonlinear phenomena can be leveraged to map microscopic spatial variations in the response of different material structures, enabling suppression of the background associated with linear scattering through spectral filtering^{2–4}. However, the spatial resolution of these methods is fundamentally limited by diffraction to approximately half the light wavelength. One approach to overcoming this problem involves the use of localized optical fields, such as those scattered from sharp tips^{5,6}, which, in addition, can enhance the near-field strength and, therefore, dramatically increase the nonlinearly scattered signal^{7–9}. Nevertheless, the introduction of external nanostructures generally perturbs the intrinsic response of the specimen.

A less conventional way of generating nonlinear signals consists in mixing external light with the broadband evanescent field accompanying a swift electron. In this work, we explore this possibility as a means to perform spectromicroscopy with a combination of high spectral and spatial resolutions. Specifically, we envision the illumination and detection of visible and near-infrared (vis-NIR) light to probe an *idle* free-electron field in the mid- and far-infrared spectral ranges. This phenomenon could be investigated in electron microscopes equipped with external illumination capabilities, which are becoming increasingly popular in the context of ultrafast electron microscopy^{10–17}.

Low-frequency excitations are commonly accessed by far-field FTIR and THz time-domain spectroscopy, which offer broadband coverage down to the mid/far-IR but are diffraction-limited to a micrometer-scale resolution^{18,19}. Scattering-type scanning near-field optical microscopy (s-SNOM) and related spectroscopies (including

¹ICFO–Institut de Ciències Fotòniques, The Barcelona Institute of Science and Technology, Castelldefels (Barcelona), Spain. ²ICREA–Institut Català de Recerca i Estudis Avançats, Barcelona, Spain. ³Present address: POLIMA–Center for Polariton-driven Light–Matter Interactions, University of Southern Denmark, Odense M, Denmark. ✉e-mail: javier.garciadeabajo@nanophotonics.es

tip-enhanced and photothermal implementations) overcome the diffraction limit via localized fields, routinely reaching a spatial resolution of tens of nanometers at the cost of placing a tip near the sample^{20–22}. Surface second-order nonlinear optics has also been shown to achieve monolayer sensitivity^{23,24}, although it is limited by diffraction, weak signals, and the presence of a nonresonant background, requiring mid/far-IR sources and careful filtering. In contrast, electron beams (e-beams) offer a less invasive approach to achieving a high spatial resolution in electron microscopes, as they can be focused down to sub-ångström regions^{25,26}. These probes permit electron energy-loss spectroscopy (EELS) to be performed²⁷, rendering information on the excitation modes in a specimen with a state-of-the-art spectral resolution of a few meV^{28,29}. However, EELS requires thin samples that are transparent to electrons, and it cannot resolve far-infrared excitations because they are overshadowed by the tail of the so-called zero-loss peak. The cathodoluminescence (CL) emission originating from linear scattering of the evanescent electron field provides an alternative spectromicroscopy method that can be applied to thicker samples, combined with a high spectral resolution through the determination of the emitted light wavelength³⁰. Nevertheless, CL spectroscopy suffers from a low signal-to-noise ratio due to the relatively low photon emission probability compared to energy-loss events. In addition, the detection of low-frequency photons remains challenging because of the poor efficiency of current detectors.

In photon-induced near-field electron microscopy^{10–16} (PINEM), electron spectra are recorded to reveal the absorption or emission of multiple photons as the electrons traverse the near field of an illuminated specimen. A similar effect has been used in electron energy-gain spectroscopy (EEGS) to achieve a combination of high spectral and spatial resolutions by scanning the frequency of the incident light^{31–38}. Additionally, spectral asymmetries in the observed electron energy sidebands associated with different numbers of exchanged photons have been claimed to provide information on the nanoscale nonlinear optical response of the specimen³⁹. These methods rely on the ability to identify spectral features in the transmitted electrons, which lie beyond the capabilities of current electron spectroscopy for far-infrared excitations. Alternatively, stimulated electron–light schemes with optical readout have been proposed, such as electron- and light-induced stimulated Raman (ELISR), where an electron-excited plasmonic near field is intended to produce a Stokes feature in the presence of an optical pump⁴⁰. While this technique avoids the need for low-frequency detectors or high-resolution electron spectrometers, it requires a large Raman response as well as optical background suppression, which have so far escaped experimental demonstration.

Here, we introduce wave-mixing cathodoluminescence (WMCL) as a disruptive approach for performing spectromicroscopy of low-frequency excitations, based on the nonlinear interaction between external light and the evanescent field of free electrons. Upon illumination with monochromatic light, WMCL arises from the nonlinear response of a specimen, producing outgoing light components with frequency shifts corresponding to energy losses and gains experienced by the electrons. When these frequency shifts coincide with resonances in the specimen, the electron field is enhanced and imprints distinct spectral features onto the nonlinearly scattered light. Considering a silver nanorod coated with retinal, we theoretically demonstrate that this method can reveal spectral information on the far-infrared vibrational fingerprints of this molecule through optical illumination and detection in the visible range. We further present a tutorial description of this unconventional wave mixing process for small, non-centrosymmetric particles exhibiting a nonlinear bulk response. Beyond its fundamental interest as a previously unexplored phenomenon, WMCL provides a unique opportunity to map low-frequency modes by avoiding the low efficiency of optical detectors in

such a spectral range and only relying on visible-light illumination and detection.

Results

Theoretical framework

We consider a nanostructure simultaneously exposed to external monochromatic light of frequency ω_{pump} and a focused e-beam passing through or near the material, as depicted in Fig. 1. Wave mixing between light and the evanescent electron field can take place, assisted by the nonlinear response of the specimen and giving rise to WMCL. This phenomenon manifests in the emission of photons with an output frequency ω_{WM} resulting from a linear combination of ω_{pump} and the different frequency components ω of the electron field. WMCL at the lowest (second) order can be anticipated to comprise three different possible channels, as summarized in Fig. 1:

- (i) sum-frequency generation (SFG): $\omega_{\text{WM}} = \omega_{\text{pump}} + \omega$ (Fig. 1, top);
- (ii) difference-frequency generation at low electron frequencies (DFG₁): $\omega_{\text{WM}} = \omega_{\text{pump}} - \omega$ for $\omega < \omega_{\text{pump}}$ (Fig. 1, middle);
- (iii) difference-frequency generation at high electron frequencies (DFG₂): $\omega_{\text{WM}} = \omega - \omega_{\text{pump}}$ for $\omega > \omega_{\text{pump}}$ (Fig. 1, bottom).

To map far-infrared modes (i.e., low ω 's) using visible light, only channels (i) and (ii) need to be considered, but we retain channel (iii) in our analysis for completeness.

We introduce the external light as a plane wave of wave vector \mathbf{k}_{pump} , with $k_{\text{pump}} = \omega_{\text{pump}}/c$, and an electric field distribution $\mathbf{E}_{\text{pump}}^{\text{ext}} e^{i(\mathbf{k}_{\text{pump}} \cdot \mathbf{r} - \omega_{\text{pump}} t)} + \text{c.c.}$, where $\mathbf{E}_{\text{pump}}^{\text{ext}}$ is the amplitude of the incident field. Upon interaction with the structure, the linear optical field can be written as $\mathbf{E}_{\text{pump}}(\mathbf{r}) e^{-i\omega_{\text{pump}} t} + \text{c.c.}$, exhibiting a more involved spatial dependence of the total field amplitude $\mathbf{E}_{\text{pump}}(\mathbf{r})$.

Without loss of generality, electrons are considered to move with velocity $\mathbf{v} = v \hat{\mathbf{z}}$ within an e-beam focused at a transverse position \mathbf{R}_0 in the $x - y$ plane. The external electric field associated with an electron has a broadband distribution that can be decomposed as $\mathbf{E}_{\text{electron}}^{\text{ext}}(\mathbf{r}, t) = (2\pi)^{-1} \int d\omega \mathbf{E}_{\text{electron}}^{\text{ext}}(\mathbf{r}, \omega) e^{-i\omega t}$ in terms of the frequency-resolved components²⁷

$$\mathbf{E}_{\text{electron}}^{\text{ext}}(\mathbf{r}, \omega) = \frac{2ie\omega}{v^2 \gamma^2} e^{i\omega z/v} \left[K_0(\zeta) \hat{\mathbf{z}} + i\gamma K_1(\zeta) \hat{\mathbf{b}} \right],$$

where $\gamma = 1/\sqrt{1 - v^2/c^2}$ is the Lorentz factor, K_0 and K_1 are modified Bessel functions evaluated at $\zeta = \omega b/v\gamma$ with $\mathbf{b} = \mathbf{R} - \mathbf{R}_0$, and we introduce the notation $\mathbf{r} = (\mathbf{R}, z)$ with $\mathbf{R} = (x, y)$. We disregard electron recoil (i.e., \mathbf{v} is assumed to be constant) as a safe approximation for the energetic e-beams under consideration. The self-consistent linear electron field $\mathbf{E}_{\text{electron}}(\mathbf{r})$ generally has a more complex spatial dependence once the interaction with the specimen is accounted for.

The material responds with a nonlinear polarization density $\mathbf{P}_{\text{WMCL}}(\mathbf{r})$ at different output frequencies ω_{WM} according to¹

$$\mathbf{P}_{\text{WMCL}}^{\nu}(\mathbf{r}, \omega_{\text{WM}}) = \begin{cases} \chi^{(2)}(\mathbf{r}, \omega_{\text{pump}}, \omega, \omega_{\text{WM}}) : \mathbf{E}_{\text{pump}}(\mathbf{r}) \mathbf{E}_{\text{electron}}(\mathbf{r}, \omega), & \nu = \text{SFG} \\ \chi^{(2)}(\mathbf{r}, \omega_{\text{pump}}, -\omega, \omega_{\text{WM}}) : \mathbf{E}_{\text{pump}}(\mathbf{r}) \mathbf{E}_{\text{electron}}^*(\mathbf{r}, \omega) \Theta(\omega_{\text{pump}} - \omega), & \nu = \text{DFG}_1 \\ \chi^{(2)}(\mathbf{r}, -\omega_{\text{pump}}, \omega, \omega_{\text{WM}}) : \mathbf{E}_{\text{pump}}(\mathbf{r}) \mathbf{E}_{\text{electron}}(\mathbf{r}, \omega) \Theta(\omega - \omega_{\text{pump}}), & \nu = \text{DFG}_2 \end{cases} \quad (1)$$

where $\chi^{(2)}$ is the position- and frequency-dependent second-order susceptibility tensor corresponding to the three different WMCL channels under consideration, indexed by ν , and the step function $\Theta(x)$ is defined as 1 for $x \geq 0$ and 0 otherwise. The WMCL field amplitude can be written as $\mathbf{E}_{\text{WM}}^{\nu}(\mathbf{r}, t) = (2\pi)^{-1} \int d\omega_{\text{WM}} \mathbf{E}_{\text{WM}}^{\nu}(\mathbf{r}, \omega_{\text{WM}}) e^{-i\omega_{\text{WM}} t}$, where the integral over ω_{WM} indicates that it inherits a broadband character from the field of the electron (i.e., from the integral over ω). The frequency-resolved emission amplitude must then incorporate the linear response of the structure at each output frequency ω_{WM} , which is captured by the electromagnetic Green tensor $\mathcal{G}(\mathbf{r}, \mathbf{r}', \omega_{\text{WM}})$, defined by

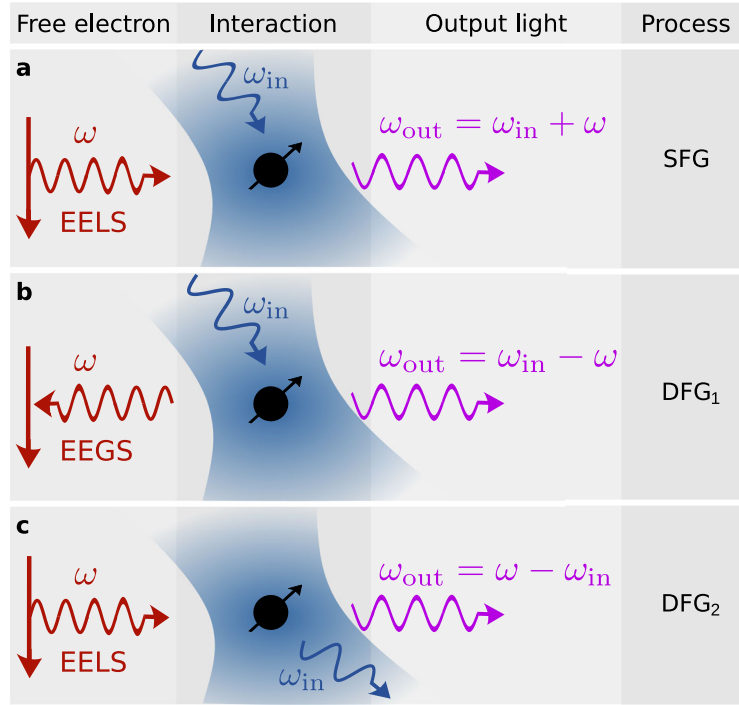


Fig. 1 | Wave mixing cathodoluminescence (WMCL). **a** We consider a specimen simultaneously exposed to light and free-electron fields. The schemes illustrate different WMCL processes involving incident photons of frequency ω_{pump} and the electromagnetic field component of frequency ω produced by a passing electron. The interaction is mediated by the nonlinear second-order susceptibility $\chi^{(2)}$ of a

specimen, giving rise to inelastically scattered photons with an output frequency $\omega_{WM} > 0$. We identify three different WMCL channels: (top) sum-frequency generation (SFG), with $\omega_{WM} = \omega_{pump} + \omega$; and (middle and bottom) difference-frequency generation, with either **(b)** $\omega_{WM} = \omega_{pump} - \omega$ (DFG₁) or **(c)** $\omega_{WM} = \omega - \omega_{pump}$ (DFG₂) for $\omega_{pump} > \omega$ or $\omega_{pump} < \omega$, respectively.

ref. 41

$$\nabla \times \nabla \times \mathcal{G}(\mathbf{r}, \mathbf{r}', \omega_{WM}) - k_{WM}^2 \mathcal{G}(\mathbf{r}, \mathbf{r}', \omega_{WM}) = 4\pi k_{WM}^2 \delta(\mathbf{r} - \mathbf{r}'),$$

where $k_{WM} = \omega_{WM}/c$. More precisely,

$$\mathbf{E}_{WM}^\nu(\mathbf{r}, \omega_{WM}) = \int_V d^3\mathbf{r}' \mathcal{G}(\mathbf{r}, \mathbf{r}', \omega_{WM}) \cdot \mathbf{P}_{WM}^\nu(\mathbf{r}', \omega_{WM}),$$

where we introduce the nonlinear polarization density defined in Eq. (1). In the far field, the output electric field becomes $\mathbf{E}_{WM}^\nu(\mathbf{r}, \omega_{WM}) \approx \mathbf{f}_{WM}^\nu(\Omega_{\hat{r}}) e^{ik_{WM}r}/r$, where $\Omega_{\hat{r}}$ denotes the emission direction \hat{r} and

$$\mathbf{f}_{WM}^\nu(\Omega_{\hat{r}}) = \int_V d^3\mathbf{r}' g(\Omega_{\hat{r}}, \mathbf{r}', \omega_{WM}) \cdot \mathbf{P}_{WM}^\nu(\mathbf{r}', \omega_{WM}) \quad (2)$$

is the far-field WMCL amplitude. In these expressions, the \mathbf{r}' integral extends over the volume V occupied by the nonlinear material, and the kernel in Eq. (2) is implicitly defined by the far-field limit ($k_{WM}r \gg 1$) of the Green tensor $\mathcal{G}(\mathbf{r}, \mathbf{r}', \omega_{WM}) \approx g(\Omega_{\hat{r}}, \mathbf{r}', \omega_{WM}) e^{ik_{WM}r}/r$. For a given emission direction, we use the reciprocity principle to conveniently obtain $g(\Omega_{\hat{r}}, \mathbf{r}', \omega_{WM})$ from the near field produced by an incident light plane wave (see Methods). We note that Eq. (2) includes phase matching implicitly through the Green tensor, which rigorously accounts for wave propagation.

We calculate the nonlinearly emitted energy by integrating the far-field Poynting vector over time and emission directions $\Omega_{\hat{r}}$. Plancherel's theorem transforms the time integral into a frequency integral, which allows us to separate the emitted energy into frequency components. After dividing each of those components by the photon energy, we finally obtain the total emission probability

as²⁷ $\Gamma_{WM}^\nu = \int_0^\infty d\omega_{WM} \Gamma_{WM}^\nu(\omega_{WM})$, where

$$\Gamma_{WM}^\nu(\omega_{WM}) = \frac{c}{4\pi^2 \hbar \omega_{WM}} \int d\Omega_{\hat{r}} |\mathbf{f}_{WM}^\nu(\Omega_{\hat{r}})|^2 \quad (3)$$

is the probability distribution for emitting WMCL photons normalized per electron and unit of photon frequency ω_{WM} for each of the three channels $\nu = \text{SFG, DFG}_1, \text{and DFG}_2$ under consideration [see Eq. (1) and Fig. 1].

Light–electron wave mixing in a small particle

As a tutorial configuration, we study a specimen consisting of a spherical particle of small radius a made of a homogeneous, non-centrosymmetric material, such that it exhibits a bulk second-order nonlinearity. For simplicity, we only consider the dipolar response for a field orientation and geometry as depicted in Fig. 2a, with a nonlinear polarization density $\mathbf{P}_{WM} = P_{WM} \hat{x}$ associated with the xxx component of the second-order susceptibility tensor $\chi^{(2)}$.

We adopt the electrostatic limit (assuming that a is small compared with the relevant optical wavelengths) and describe the material through a generic Drude-Lorentz permittivity

$$\epsilon(\omega) = 1 + f\omega_r^2 / [\omega_r^2 - \omega(\omega + i\eta)], \quad (4)$$

where f is a dimensionless factor, ω_r is an intrinsic resonance frequency, and η is an inelastic damping rate. The optical and electron fields inside the particle are then uniform and approximately given by the external fields at the sphere center times a factor $3/(\epsilon + 2)$ evaluated at the frequencies ω_{pump} and ω , respectively. The near field is thus enhanced under the condition $\epsilon = -2$, or equivalently, when the frequency approaches the sphere resonance $\omega_0 = \omega_r \sqrt{1+f/3}$, as obtained by directly applying Eq. (4). Likewise, the kernel of Eq. (2) reduces to $g(\Omega_{\hat{r}}, \mathbf{r}', \omega_{WM}) = (3k_{WM}^2 / [\epsilon(\omega_{WM}) + 2]) (1 - \hat{r} \otimes \hat{r})$ in the electrostatic

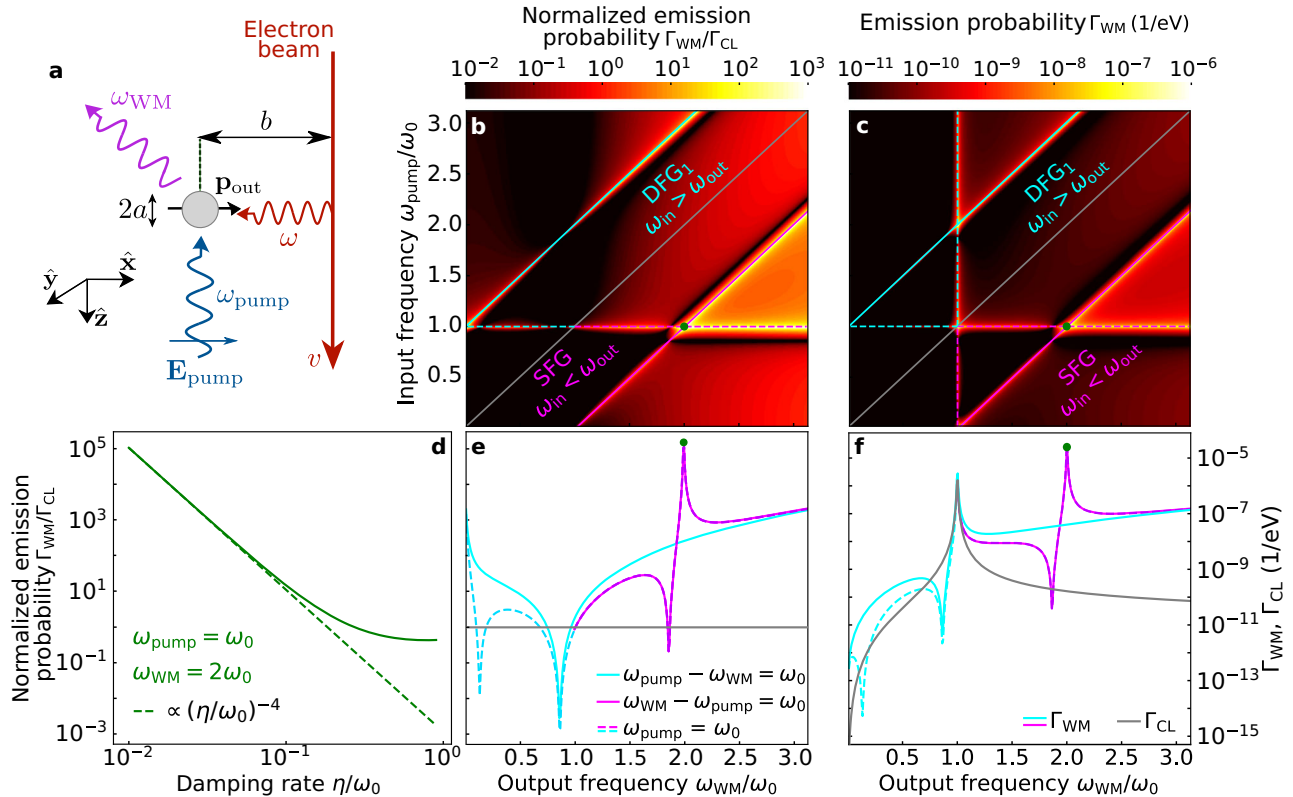


Fig. 2 | WMCL and WM by a small particle. **a** Sketch of the geometry under consideration, including a spherical particle of radius a that features a dipolar resonance at frequency ω_0 . The electron moves with velocity v and passes at a distance b from the particle center. The directions of electron and light propagation are indicated by arrows relative to the lower-left frame. **b** Probability of nonlinear WM photon emission Γ_{WM}^{ν} normalized to Γ_{CL} as a function of incident and output frequencies ω_{pump} and ω_{WM} normalized to ω_0 . The solid gray line divides regions of $v = SFG$ ($\omega_{WM} = \omega_{pump} + \omega$) and $v = DFG_1$ ($\omega_{WM} = \omega_{pump} - \omega$) emission (see labels). Pink and blue lines mark the main emission features. **c** Same as (b), but for

the probability of nonlinear WM photon emission Γ_{WM}^{ν} without normalizing to CL. **d** Dependence of Γ_{WMCL}^{SFG} on damping η for ω_{pump} and ω_{WM} at the green dot in (b) (solid curve), compared with a $\propto \eta^{-4}$ dependence (dashed line). **e, f** Cuts of panels (b, c) along the color-coordinated lines (see legends). The gray solid curves represent the CL photon emission probability Γ_{CL} . We set $\chi^{(2)} = 10^{-10}$ m/V, $E_{pump} = 10^8$ V/m, $a = 10$ nm, $b = 12$ nm, $v = c/10$ (2.6 keV), $f = 1$, $\omega_0 = 0.1$ eV, and $\eta/\omega_0 = 0.01$ in all panels [see Eqs. (4)–(6)]. In panels (b, c), the minimum and maximum values on the color maps are saturated to the values indicated in the corresponding legends.

limit (see Methods). Inserting these elements in Eqs. (2) and (3), the WMCL emission probability directly becomes

$$\Gamma_{WM}^{\nu}(\omega_{WM}) = 3888 \alpha V^2 I^{\text{ext}} |\chi^{(2)}|^2 \frac{\omega_{WM}^3 \omega^2}{c^3 v^4 \gamma^2} K_1^2 \left(\frac{\omega b}{v \gamma} \right) \times \frac{1}{|[\epsilon(\omega_{pump}) + 2][\epsilon(\omega_{WM}) + 2][\epsilon(\omega) + 2]|^2}, \quad (5)$$

where $I^{\text{ext}} = (c/2\pi)|E_{pump}|^2$ is the incident light intensity, $V = 4\pi a^3/3$ is the particle volume, $\alpha = e^2/\hbar c \approx 1/137$ is the fine structure constant, and b is the e-beam distance to the particle center (see Fig. 2a). We consider only aloof electron trajectories that do not penetrate the sampled material. A nonlinear emission channel ν is selected through the choice of ω_{WM} and the frequency parameters of $\chi^{(2)}$ [see Eq. (1)]. Incidentally, from this analysis, it is clear that the WMCL probability scales as $\propto |\chi^{(2)}|^2 I^{\text{ext}}$.

Since both regular CL and WMCL can give rise to the emission of photons with the same frequency, the ratio of their respective probabilities becomes a relevant quantity that we explore in Fig. 2. The CL probability is also given by Eqs. (2) and (3), but taking $\omega_{WM} = \omega$ and writing the polarization density as $\mathbf{P}_{WM}^{\text{ext}}(\mathbf{r}', \omega) = \mathbf{E}_{\text{electron}}(-b\hat{\mathbf{x}}, \omega)[\epsilon(\omega) - 1]/4\pi$ from the linear response to the electron field. This leads to

$$\Gamma_{CL}(\omega) = \frac{3\alpha V^2 \omega^5}{2\pi^3 c^2 v^4 \gamma^2} \left| \frac{\epsilon(\omega) - 1}{\epsilon(\omega) + 2} \right|^2 \left[K_1^2 \left(\frac{\omega b}{v \gamma} \right) + \frac{1}{\gamma^2} K_0^2 \left(\frac{\omega b}{v \gamma} \right) \right], \quad (6)$$

which agrees with previous analyses⁴².

Figure 2b shows the $\Gamma_{WM}^{\nu}(\omega_{WM})/\Gamma_{CL}(\omega_{WM})$ ratio as a function of input and output light frequencies (ω_{in} and ω_{WM}) for the $\nu = SFG$ ($\omega_{WM} > \omega_{pump}$) and $\nu = DFG_1$ ($\omega_{pump} > \omega_{WM}$) channels, assuming a particle resonance $\hbar\omega_0 = 0.1$ eV, such that the e-beam can produce strong frequency shifts with a large probability (see also Supp. Fig. S1). Figure 2c shows the same data without normalization to the CL intensity, assuming typical orders of magnitude for the values of $\chi^{(2)} \sim 10^{-10}$ m/V⁴³ (see Table S1 in the Supplementary Information) and $E_{pump} \sim 10^8$ V/m. In particular, this value for E_{pump} is routinely reached in nonlinear experiments using short pulses (100s fs) without causing sample damage^{44–46}. In both panels, we can identify some lines where the WMCL emission is boosted (marked in pink/red for SFG/DFG₁ channels; see also cuts along these lines in Fig. 2e). These features correspond to resonances marked by the condition $\epsilon + 2 \approx 0$ in the denominator of Eq. (5) when either $\omega_{pump} = \omega_0$ (horizontal line) or $\omega = \omega_0$ (oblique lines). Note that the $\omega_{WM} = \omega_0$ resonance is removed in the $\Gamma_{WM}^{\nu}/\Gamma_{CL}$ ratio because Γ_{CL} is also peaked at that frequency [see Eq. (6)]. For completeness, Supp. Fig. S1 shows $\Gamma_{DFG_2}(\omega_{WM})/\Gamma_{CL}(\omega_{WM})$ and $\Gamma_{DFG_2}(\omega_{WM})$ for the alternative channel where $\omega_{WM} = \omega - \omega_{pump}$, which also exhibits resonances at $\omega_{pump} = \omega_0$ and $\omega_{pump} + \omega_{WM} = \omega_0$ (dashed and solid lines). Cuts along these lines in Supp. Figs. S1c, d reveal a behavior similar to that of DFG₁ in Fig. 2e,f, respectively. Finally, we note that the apparent increase of Γ_{WM}/Γ_{CL} with ω_{WM} in Figs. 2b,e (and Γ_{WM} in Fig. 2c,f) originates from a broad high-energy resonance associated with $\omega_{WM}^3 \omega^2 K_1^2(\omega b/v\gamma)$ in Eq. (5).

The boosts of WMCL induced by material resonances are strongly dependent on optical damping [η in Eq. (4)]. For the specific form of the permittivity in Eq. (4), each resonant denominator ($|\epsilon + 2|^2 \approx 0$) in the WMCL probability [Eq. (1)] contributes a factor $\propto (\omega_0/\eta)^2$. In particular, at the double-resonance crossing signaled by the green dot in Fig. 2b (DFG₁ with $\omega_{\text{pump}} = \omega = \omega_0$), we expect a $\Gamma_{\text{WM}}^{\text{DFG}_1} \propto \eta^{-4}$, as corroborated by Fig. 2d.

We present above WMCL probabilities normalized to CL because photons generated by these two processes cannot be directly distinguished in an experiment. However, unlike CL, the WMCL contribution is proportional to the intensity of the external pump I_{ext} , and thus, it can be resolved by switching the external illumination on and off (e.g., in a lock-in amplifier). In Supplementary Fig. S2, we show both Γ_{WM} (summed over all nonlinear processes), Γ_{CL} , and their sum as a function of the output light frequency ω_{WM} , for $\omega_{\text{pump}} = \omega_0$ and different values of E_{pump} . Additional channels not present in this figure correspond to the direct pump field scattered by the sample and its harmonics, which can be experimentally removed by filtering (analogously to the suppression of Rayleigh scattering in Raman scattering). In addition, the WMCL and pump-scattered signals generally exhibit different far-field angular and polarization patterns, suggesting that they could be angularly separated (e.g., using directional nanoantennas). Finally, harmonics of the electron field are also allowed, but we expect them to be too weak to be measurable.

While in Fig. 2 we maintain the analysis general for tutorial purposes, the results therein presented are readily applicable to nonlinear materials that are non-centrosymmetric (and therefore exhibit a non-zero bulk $\chi^{(2)}$) and whose permittivity is well described by the Drude-Lorentz model in Eq. (4). For example, we show in Supp. Table S1 a representative list of materials fitting these criteria, for which the results in this section readily apply. The table contains the material-dependent orders of magnitude of $\chi^{(2)}$ within different spectral ranges^{47–55}, along with references for fitting parameters of the Drude-Lorentz permittivity^{56–64}. We note that a straightforward extension of the present theory can deal with permittivities constructed as a sum of multiple Lorentz oscillators, which can be more accurate for some of the materials in Supp. Table S1.

Detection of far-infrared molecular fingerprints in a plasmonic nanoparticle

We are interested in extending the WMCL analysis to a specimen hosting multiple resonances, and in particular, one at high energy supported by a metallic nanoparticle (enhancing the overall WMCL signal for input and output light in the visible domain), and another one at low frequency (down to the far infrared), driven by molecular fingerprints of an analyte. As a practical implementation of this idea, we consider a metallic particle coated with a molecular layer of retinal. The particle is aimed at producing a strong near-field enhancement of incident light at a visible resonant frequency. In contrast, the broadband electron field extends down to low frequencies and can be enhanced by the response of the molecules. The output WMCL signal should then be boosted for ω_{pump} and ω_{WM} close to a nanorod resonance, while its fine structure should reveal features at frequency shifts $\omega_{\text{WM}} - \omega_{\text{pump}}$ corresponding to the molecular fingerprints.

We take a silver nanorod (length $L = 100$ nm, radius $a = 10$ nm, hemispherical caps) covered by a layer of retinal (thickness $t = 5$ nm), as schematically sketched in Fig. 3a. The system is illuminated by a light plane wave of frequency ω_{pump} . An electron with velocity v passes near the structure as indicated in Fig. 3a. We focus on the SFG and DFG₁ processes by which the electron gains or loses an amount of energy $\hbar\omega$ upon interaction with the sample, which results in the emission of a photon of frequency $\omega_{\text{WM}} = \omega_{\text{pump}} \pm \omega$. Since silver is a centrosymmetric material, its second-order nonlinear response is only coming from the nanorod surface, and is quantified by a nonlinear surface susceptibility $\chi^{(2)}$ for which we only retain the dominant $\perp\perp\perp$

component. Symmetry breaking in the applied electric field is produced by the position of the electron, near one of the ends of the structure. In our analysis, we use the boundary-element method⁶⁵ (BEM) to calculate the self-consistent linear fields produced by the light and the electron, from which we obtain the WMCL probability through Eqs. (2) and (3) (see Methods).

In Fig. 3b, we present the CL spectrum of the structure in Fig. 3a, exhibiting a strong dipolar resonance that shifts due to the presence of the retinal layer. For WMCL, we take the incident light frequency ω_{pump} to match the maximum of the resonance in this plot for a given layer thickness. In Fig. 3c, we show the probability of emitting SFG and DFG photons as a function of electron energy change, normalized to both the CL emission probability and the dimensionless parameter $\xi^2 = |\chi_{\perp\perp\perp}^{(2)} E_{\text{pump}}|^2/A$, where A is the surface area of the nanorod. In Supplementary Fig. S3a, we present the same results without normalization, while in Supplementary Fig. S3b, we show analogous calculations, but for a silica coating instead of retinal. In all cases, we use an attainable pump field amplitude $E_{\text{pump}} = 10^8$ V/m (see discussion above) and $\chi_{\perp\perp\perp}^{(2)} \sim 4 \times 10^{-16}$ m²/V. The latter results from extrapolating the measured visible-range second-harmonic susceptibility for silver^{66,67} to the lower-frequency range here considered (see Methods). We concentrate on the electron energy loss and gain region in the -8 to 8 meV range [that is, in terms of the electron frequency $\omega = \pm (\omega_{\text{WM}} - \omega_{\text{pump}})$], where retinal exhibits strong vibrational resonances. Such resonances are imprinted onto the WMCL spectrum of the structure with retinal, emerging as weak modulations in the normalized emission probability, which are instead absent from the spectrum for the bare nanorod. Note that, in contrast, the CL spectrum (without external illumination) to which we are normalizing the WMCL signal in this energy range is dominated by the silver nanorod, so it is featureless even in the presence of a retinal layer, which only produces a nearly rigid redshift of the plasmon resonance (Fig. 3b). The modulations in probability produced by the retinal vibrational modes on the WMCL spectrum (Supplementary Fig. S3a) have a similar order of magnitude as the CL peak (Fig. 3b), and although they are clearly visible, to make such features more prominent, we take the derivatives of the WMCL spectra with respect to $\omega = |\omega_{\text{WM}} - \omega_{\text{pump}}|$, and compare the result to the absorption spectrum of retinal (Fig. 3d), finding excellent agreement.

The WMCL signal can be improved by adequately choosing the electron trajectory to traverse the near-field hotspots produced upon illumination of the sample, as shown by the spatial map in Supplementary Fig. S4. This method can also be applied to other types of analytes. For example, for a silver nanorod coated with a thin silica layer, we find analogous features associated with vibrational resonances in the mid-infrared spectral range (see Supplementary Figs. S3b and S5). We thus conclude that WMCL is capable of identifying the chemical nature of analytes characterized by low-frequency spectral fingerprints by resorting to external illumination and light detection in the visible regime.

Discussion

In conclusion, we show that free electrons can be combined with light to produce WMCL and map low-frequency optical excitations by triggering a nonlinear response associated with sum- and difference-frequency generation. Unlike other low-frequency spectroscopy techniques, WMCL benefits from the broadband character of the field carried by fast electrons while up-converting far-infrared fingerprints to the visible, eliminating the need for low-frequency light sources and detectors, and thus, enabling spectroscopy with standard visible-range optical detectors in nanoscale specimens. This method can thus resolve far-infrared features with nanometer resolution, for which no other technique is available. Although we have considered uniform molecular coatings for simplicity, in a practical situation, WMCL could be applied to examining inhomogeneous molecular distributions,

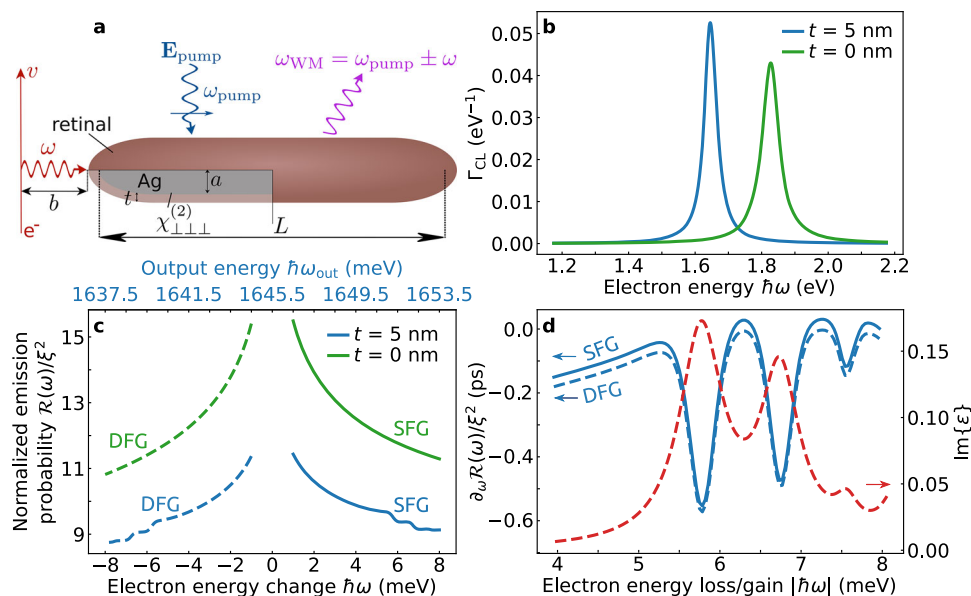


Fig. 3 | Probing low-energy excitations through WMCL. **a** Scheme of the structure under consideration, consisting of a silver nanorod (length $L = 100$ nm, radius $a = 10$ nm) coated by a retinal layer (thickness t). The structure is irradiated by a light plane wave of frequency ω_{pump} and polarization along the rod. The electron moves with a velocity $v = 0.45c$ and passes at a distance $b = 3$ nm from one end of the coated rod. SFG and DFG produce output photon energies $\omega_{\text{WM}} = \omega_{\text{pump}} \pm \omega$ through the second-order susceptibility $\chi_{\perp\perp\perp}^{(2)}(\omega_{\text{pump}}, \pm\omega, \omega_{\text{WM}})$ at the silver surface. **b** CL spectra for bare ($t = 0$) and coated ($t = 5$ nm) silver nanorods under the geometry depicted in **(a)**. **c** Normalized probability of SFG and DFG photon

emission as a function of electron energy change. We plot the quantity $\mathcal{R}(\omega)/\xi^2$ for bare and retinal-coated nanorods, with $\mathcal{R}(\omega) = \Gamma_{\text{SFG/DFG}}(\omega_{\text{WM}})/\Gamma_{\text{CL}}(\omega_{\text{WM}})$, $\omega = \pm(\omega_{\text{WM}} - \omega_{\text{pump}})$, and $\xi^2 = |\chi_{\perp\perp\perp}^{(2)} E_{\text{pump}}|^2/A$ combining the surface area of the nanorod $A = 2\pi aL$ and the incident light-field amplitude E_{pump} . The upper horizontal scale indicates the output photon energy for the retinal-coated nanorod (blue curve), with the bare-nanorod counterpart (green curve) shifted by $+184.5$ meV. **d** Comparison of $\partial_{\omega}\mathcal{R}(\omega)$ to the imaginary part of the permittivity of retinal as a function of absolute electron frequency change $\omega = |\omega_{\text{WM}} - \omega_{\text{pump}}|$.

benefiting from the tightly confined electron field. In addition, WMCL is not limited to molecular vibrations, as the same wave-mixing principle applies to other low-frequency excitations, such as phonon-polaritons in the Reststrahlen bands of polaritonic materials (as shown in Supp. Fig. S5), free-carrier plasmons in doped semiconductors or graphene, and spin excitations (THz magnons) supported, for example, by some antiferromagnets. In all cases, low-frequency modes can be up-converted to visible sidebands, similarly to our demonstration, enabling nanoscale readout with standard detectors.

The successful design of experiments based on electron-photon wave mixing requires that the output signal originating from this process is larger than (and thus distinguishable from) the regular CL emission produced in the absence of external illumination. This condition depends on the second-order nonlinear susceptibility of the specimen or a neighboring structure (e.g., retinal and a silver nanorod in our illustrative example), while in addition, the WMCL intensity is proportional to the employed light intensity. The latter can be boosted by using synchronized ultrafast electron and laser pulses similar to PINEM and EEGS. Other strategies to increase the WMCL signal could rely on near-field enhancement (e.g., via pump field focusing or engineering of sample geometry and choice of materials), improving the second-order nonlinear response of the sample (i.e., higher $\chi^{(2)}$ in optimized materials and geometries), and adjusting the electron trajectory to enhance interaction (e.g., using small impact parameters and aligning the trajectory to increase field overlap and phase matching).

Realistic candidate materials for WMCL experiments include non-centrosymmetric dielectrics with large bulk $\chi^{(2)}$ and low loss at visible pump wavelengths, such as thin-film LiNbO_3 , GaP, and III-nitrides (AlN/GaN), which are standard platforms for efficient second-harmonic/SFG and, therefore, natural targets for WMCL^{68–70}. In phonon-polaritonic dielectrics such as hBN, SiC, and $\alpha\text{-MoO}_3$, which provide strong mid-IR near-field enhancements, symmetry forbids bulk second-order

processes, thus leading to the vanishing of WMCL in the electrostatic limit (e.g., for the small particle studied in Fig. 2). However, a sizeable wave mixing could be obtained in larger particles, like in the ones explored in Fig. 3, based on their second-order surface response^{71,72}. In that direction, noble metals such as Au or Ag could be useful because they exhibit strong, well-characterized surface second-order responses at vis-NIR frequencies⁶⁷. Heavily doped semiconductors (e.g., n-GaAs) are also plasmonic mid-IR candidates, although their field enhancement at low frequencies is limited by inelastic damping^{73–76}.

Besides rendering spectral information on far-infrared excitations, WMCL should also provide quantitative measurements of the material-dependent second-order susceptibility for any of the materials listed above. Although we have restricted our analysis to second-order nonlinear processes, WMCL could also be extended to higher orders, which should become dominant in small centrosymmetric samples.

Methods

Calculation of the far-field electromagnetic Green tensor using the reciprocity principle

To calculate $g(\Omega_{\mathbf{r}}, \mathbf{r}', \omega_{\text{WM}})$ as a function of far-field emission direction $\Omega_{\mathbf{r}}$ and position \mathbf{r}' within a nanostructure, we consider a dipole $\mathbf{p} = p\hat{\mathbf{u}}_1$ oscillating with frequency ω_{WM} , placed at \mathbf{r}' , and oriented along the unit vector $\hat{\mathbf{u}}_1$. The electric field component along $\hat{\mathbf{u}}_2$ at a far-field position \mathbf{r} (with $r \gg r'$) is given by

$$\hat{\mathbf{u}}_2 \cdot \mathcal{G}(\mathbf{r}, \mathbf{r}', \omega_{\text{WM}}) \cdot \mathbf{p} \approx [\hat{\mathbf{u}}_2 \cdot g(\Omega_{\mathbf{r}}, \mathbf{r}', \omega_{\text{WM}}) \cdot \hat{\mathbf{u}}_1] p \frac{e^{ik_{\text{WM}}r}}{r}.$$

By invoking the principle of reciprocity [i.e., $\hat{\mathbf{u}}_1 \cdot \mathcal{G}(\mathbf{r}, \mathbf{r}', \omega_{\text{WM}}) \cdot \hat{\mathbf{u}}_2 = \hat{\mathbf{u}}_2 \cdot \mathcal{G}(\mathbf{r}', \mathbf{r}, \omega_{\text{WM}}) \cdot \hat{\mathbf{u}}_1$], this quantity must coincide with the $\hat{\mathbf{u}}_1$ component of the field produced at \mathbf{r}' by a distant dipole $p\hat{\mathbf{u}}_2$ placed at \mathbf{r} . We only need to consider $\hat{\mathbf{u}}_2$ directions perpendicular to \mathbf{r} because the

far field is transverse. The external field produced by such a dipole near the structure is $k_{\text{WM}}^2 \mathbf{p} \hat{\mathbf{u}}_2 e^{-ik_{\text{WM}} \mathbf{r}} e^{ik_{\text{WM}} \mathbf{r}'} / r$, where $\mathbf{k}_{\text{WM}} = k_{\text{WM}} \hat{\mathbf{r}}$. From these considerations, we formulate the following prescription to calculate the components of the tensor $g(\Omega_{\hat{\mathbf{r}}}, \mathbf{r}', \omega_{\text{WM}})$: (1) we consider a plane wave illuminating the structure with wave vector $-\mathbf{k}_{\text{WM}}$ and unit electric field amplitude $\hat{\mathbf{u}}_2$; (2) we calculate the resulting self-consistent near field $\mathbf{E}(\mathbf{r}')$ as a function of \mathbf{r}' ; (3) we then write

$$\hat{\mathbf{u}}_2 \cdot g(\Omega_{\hat{\mathbf{r}}}, \mathbf{r}', \omega_{\text{WM}}) \cdot \hat{\mathbf{u}}_1 = k_{\text{WM}}^2 \hat{\mathbf{u}}_1 \cdot \mathbf{E}(\mathbf{r}').$$

To obtain the full tensor, this procedure needs to be repeated for $\hat{\mathbf{u}}_1 = \hat{\mathbf{x}}, \hat{\mathbf{y}},$ and $\hat{\mathbf{z}}$ for all values of the emission direction, while $\hat{\mathbf{u}}_2$ can be set to the p and s unit polarization vectors corresponding to the emission direction $\Omega_{\hat{\mathbf{r}}}$.

For a sphere in the electrostatic limit, a unit incident field $\hat{\mathbf{u}}_2$ produces a uniform field $3\hat{\mathbf{u}}_2/(\epsilon + 2)$ inside the material, where ϵ is the permittivity at the frequency ω_{WM} under consideration. From this identity, applying the procedure formulated above, we directly write

$$g(\Omega_{\hat{\mathbf{r}}}, \mathbf{r}', \omega_{\text{WM}}) = \frac{3k_{\text{WM}}^2}{\epsilon + 2} (1 - \hat{\mathbf{r}} \otimes \hat{\mathbf{r}}),$$

where we have inserted $(1 - \hat{\mathbf{r}} \otimes \hat{\mathbf{r}})$ to account for the fact that the far field is transverse.

For the (coated) silver nanorod, we also follow the procedure above and calculate the near field upon plane-wave illumination using an implementation of the boundary-element method⁶⁵ specialized for axially symmetric structures.

Material permittivities

We use the tabulated permittivity of silver taken from experimental measurements⁷⁷. The permittivity of retinal is modeled as a sum of six Lorentzians⁷⁸:

$$\epsilon_{\text{retinal}}(\omega) = \epsilon_{\infty} + \sum_{j=1}^6 \frac{S_j \omega_j^2}{\omega_j^2 - \omega(\omega + i\eta_j)}, \quad (7)$$

with parameters $\epsilon_{\infty} = 2.157$, $S_1 = 0.018$, $\omega_1 = 46.6 \text{ cm}^{-1}$, $\eta_1 = 5.2 \text{ cm}^{-1}$, $S_2 = 0.011$, $\omega_2 = 54.4 \text{ cm}^{-1}$, $\eta_2 = 4.7 \text{ cm}^{-1}$, $S_3 = 0.001$, $\omega_3 = 61.0 \text{ cm}^{-1}$, $\eta_3 = 2.8 \text{ cm}^{-1}$, $S_4 = 0.002$, $\omega_4 = 66.2 \text{ cm}^{-1}$, $\eta_4 = 3.4 \text{ cm}^{-1}$, $S_5 = 0.001$, $\omega_5 = 69.3 \text{ cm}^{-1}$, $\eta_5 = 2.4 \text{ cm}^{-1}$, $S_6 = 0.008$, $\omega_6 = 90.6 \text{ cm}^{-1}$, and $\eta_6 = 4.9 \text{ cm}^{-1}$.

Nonlinear susceptibility for wave mixing of far-infrared and visible light

While literature values of $\chi_{\perp\perp\perp}^{(2)}$ for noble metals at vis-NIR frequencies are available^{66,67}, the mixing of visible and far-infrared fields remains poorly studied⁷⁹. To address this gap for the present proposal, we extrapolate vis-NIR measurements by considering the scaling of this type of process as a function of the mixed frequencies ω_1 and ω_2 (e.g., $\chi_{\perp\perp\perp}^{(2)} \propto [\omega_1(\omega_1 + \omega_2)]^{-1}$ for SFG in a metal¹). Considering typical values of $\chi_{\perp\perp\perp}^{(2)} \sim 10^{-18} \text{ m}^2/\text{V}$ for second-harmonic generation with $\hbar\omega_1 = 1.55 \text{ eV}$ light in silver^{66,67}, we expect the nonlinear susceptibility to be enhanced by approximately two orders of magnitude when one of the frequencies is shifted to the far infrared. More precisely, assuming this frequency scaling and taking $\hbar\omega_2 < 8 \text{ meV}$ while keeping ω_1 at a similar value as indicated above (i.e., under the same conditions as in Fig. 3), $\chi_{\perp\perp\perp}^{(2)}$ is expected to scale by a factor $\sim 2\omega_1/\omega_2 \sim 400$. Accordingly, we use a value $\chi_{\perp\perp\perp}^{(2)} = 4 \times 10^{-16} \text{ m}^2/\text{V}$ for wave mixing of far-infrared ($< 8 \text{ meV}$) and vis-NIR ($\sim 1.6 \text{ eV}$) light to plot the WMCL probability in Supp. Fig. S3 under the conditions of Fig. 3.

Data availability

The data that support the findings of this study are available from the corresponding author upon request.

References

- Boyd, R. W. *Nonlinear Optics*. Academic Press: Amsterdam, 2008.
- Barad, Y., Eisenberg, H., Horowitz, M. & Silberberg, Y. Nonlinear scanning laser microscopy by third harmonic generation. *Appl. Phys. Lett.* **70**, 92–924 (1997).
- Harutyunyan, H., Palomba, S., Renger, J., Quidant, R. & Novotny, L. Nonlinear dark-field microscopy. *Nano Lett.* **10**, 5076–5079 (2010).
- Blankenship, B. W. et al. Multiphoton and harmonic imaging of microarchitected materials. *ACS Appl. Mater. Interfaces* **17**, 3887–3896 (2025).
- Bouhelier, A., Beversluis, M., Hartschuh, A. & Novotny, L. Near-field second-harmonic generation induced by local field enhancement. *Phys. Rev. Lett.* **90**, 013903 (2003).
- Le Ru, E. C. & Auguié, B. Enhancement factors: A central concept during 50 years of surface-enhanced Raman spectroscopy. *ACS Nano* **18**, 9773–9783 (2024).
- Abb, M., Wang, Y., de Groot, C. H. & Muskens, O. L. Hotspot-mediated ultrafast nonlinear control of multifrequency plasmonic nanoantennas. *Nat. Commun.* **5**, 4869 (2014).
- Wang, C.-F. & El-Khoury, P. Z. Multimodal tip-enhanced nonlinear optical nanoimaging of plasmonic silver nanocubes. *J. Phys. Chem. Lett.* **12**, 10761–10765 (2021).
- Luo, Y. et al. Visualizing hot carrier dynamics by nonlinear optical spectroscopy at the atomic length scale. *Nat. Commun.* **16**, 4999 (2025).
- Barwick, B., Flannigan, D. J. & Zewail, A. H. Photon-induced near-field electron microscopy. *Nature* **462**, 902–906 (2009).
- Feist, A. et al. Quantum coherent optical phase modulation in an ultrafast transmission electron microscope. *Nature* **521**, 200–203 (2015).
- Piazza, L. et al. Simultaneous observation of the quantization and the interference pattern of a plasmonic near-field. *Nat. Commun.* **6**, 6407 (2015).
- Ryabov, A. & Baum, P. Electron microscopy of electromagnetic waveforms. *Science* **353**, 374–377 (2016).
- Kozák, M., Eckstein, T., Schönenberger, N. & Hommelhoff, P. Inelastic ponderomotive scattering of electrons at a high-intensity optical travelling wave in vacuum. *Nat. Phys.* **14**, 121–125 (2018).
- Dahan, R. et al. Imprinting the quantum statistics of photons on free electrons. *Science* **373**, eabj7128 (2021).
- Mihaila, M. C. C. et al. Transverse electron-beam shaping with light. *Phys. Rev. X* **12**, 031043 (2022).
- García de Abajo, F. J., Polman, A., Velasco, C. I. & others Roadmap for quantum nanophotonics with free electrons. *ACS Photonics* **12**, 4760–4817 (2025).
- Tonouchi, M. Cutting-edge terahertz technology. *Nat. Photonics* **1**, 97–105 (2007).
- Neu, J. & Schmuttenmaer, C. A. Tutorial: An introduction to terahertz time-domain spectroscopy (THz-TDS). *J. Appl. Phys.* **124**, 231101 (2018).
- Keilmann, F. & Hillenbrand, R. Near-field microscopy by elastic light scattering from a tip. *Philos. Trans. R. Soc. A* **362**, 787–805 (2004).
- Centrone, A. Infrared imaging and spectroscopy beyond the diffraction limit. *Annu. Rev. Anal. Chem.* **8**, 101–126 (2015).
- Huth, F. et al. Nano-FTIR absorption spectroscopy of molecular fingerprints at 20 nm spatial resolution. *Nano Lett.* **12**, 3973–3978 (2012).
- Heinz, T. F., Chen, C. K., Ricard, D. & Shen, Y. R. Spectroscopy of molecular monolayers by resonant second-harmonic generation. *Phys. Rev. Lett.* **48**, 478–481 (1982).
- Boyd, G. T., Shen, Y. R. & Hänsch, T. W. Continuous-wave second-harmonic generation as a surface microprobe. *Opt. Lett.* **11**, 97–99 (1986).
- Nellist, P. D. et al. Direct sub-angstrom imaging of a crystal lattice. *Science* **305**, 1741 (2004).

26. Muller, D. A. et al. Atomic-scale chemical imaging of composition and bonding by aberration-corrected microscopy. *Science* **319**, 1073–1076 (2008).
27. García de Abajo, F. J. Optical excitations in electron microscopy. *Rev. Mod. Phys.* **82**, 209–275 (2010).
28. Krivanek, O. L. et al. Vibrational spectroscopy in the electron microscope. *Nature* **514**, 209–214 (2014).
29. Hage, F. S., Radtke, G., Kepaptsoglou, D. M., Lazzeri, M. & Ramasse, Q. M. Single-atom vibrational spectroscopy in the scanning transmission electron microscope. *Science* **367**, 1124–1127 (2020).
30. Polman, A., Kociak, M. & García de Abajo, F. J. Electron-beam spectroscopy for nanophotonics. *Nat. Mater.* **18**, 1158–1171 (2019).
31. García de Abajo, F. J. & Kociak, M. Electron energy-gain spectroscopy. *N. J. Phys.* **10**, 073035 (2008).
32. Das, P. et al. Stimulated electron energy loss and gain in an electron microscope without a pulsed electron gun. *Ultramicroscopy* **203**, 44–51 (2019).
33. Liu, C. et al. Continuous wave resonant photon stimulated electron energy-gain and electron energy-loss spectroscopy of individual plasmonic nanoparticles. *ACS Photonics* **6**, 2499–2508 (2019).
34. Wang, K. et al. Coherent interaction between free electrons and a photonic cavity. *Nature* **582**, 50–54 (2020).
35. Pomarico, E. et al. meV resolution in laser-assisted energy-filtered transmission electron microscopy. *ACS Photonics* **5**, 759–764 (2018).
36. Henke, J.-W. et al. Integrated photonics enables continuous-beam electron phase modulation. *Nature* **600**, 653–658 (2021).
37. Auad, Y. et al. μeV electron spectromicroscopy using free-space light. *Nat. Commun.* **14**, 4442 (2023).
38. Müller, N. et al. <https://doi.org/10.48550/arXiv.2405.12017> “Spectrally resolved free electron-light coupling strength in a transition metal dichalcogenide”, <http://arxiv.org/abs/2405.12017> arXiv:2405.12017 (2024).
39. Konečná, A., Di Giulio, V., Mkhitarian, V., Ropers, C. & García de Abajo, F. J. Nanoscale nonlinear spectroscopy with electron beams. *ACS Photonics* **7**, 1290–1296 (2020).
40. Saleh, A. mrA. E., Angell, D. K. & Dionne, J. A. Electron- and light-induced stimulated Raman spectroscopy for nanoscale molecular mapping. *Phys. Rev. B* **102**, 085406 (2020).
41. Novotny, L., Hecht, B. Principles of Nano-optics. Cambridge University Press: New York, 2006.
42. García de Abajo, F. J. & Di Giulio, V. Optical excitations with electron beams: challenges and opportunities. *ACS Photonics* **8**, 945–974 (2021).
43. Iyikanat, F., Konečná, A., García de Abajo, F. J., Mortensen, N. A. & Cox, J. D. Nonlinear tunable vibrational response in hexagonal boron nitride. *ACS Nano* **15**, 13415–13426 (2021).
44. Liu, D., Ren, Y., Huo, Y., Cai, Y. & Ning, T. Second harmonic generation in plasmonic metasurfaces enhanced by symmetry-protected dual bound states in the continuum. *Opt. Express* **31**, 23127–23139 (2023).
45. Sakurai, A., Takahashi, S., Mochizuki, T. & Sugimoto, T. Tip-enhanced sum frequency generation for molecular vibrational nanospectroscopy. *Nano Lett.* **25**, 6390–6398 (2025).
46. Zhao, Y. et al. Second-harmonic generation in strained silicon metasurfaces. *Adv. Photon. Res.* **3**, 2200157 (2022).
47. Skauli, T. et al. Measurement of the nonlinear coefficient of orientation-patterned GaAs and demonstration of highly efficient second-harmonic generation. *Opt. Lett.* **27**, 628–630 (2002).
48. Shoji, I., Kondo, T., Kitamoto, A., Shirane, M. & Ito, R. Absolute scale of second-order nonlinear-optical coefficients. *J. Opt. Soc. Am. B* **14**, 2268–2294 (1997).
49. Insero, G. et al. Mid-infrared tunable, narrow-linewidth difference-frequency laser based on orientation-patterned gallium phosphide. *J. Phys. Conf. Ser.* **793**, 012012 (2017).
50. Wagner, H. P., Kühnelt, M., Langbein, W. & Hvam, J. M. Dispersion of the second-order nonlinear susceptibility in ZnTe, ZnSe, and ZnS. *Phys. Rev. B* **58**, 10494–10501 (1998).
51. Irmer, G., Röder, C., Himcinschi, C. & Kortus, J. Nonlinear optical coefficients of wurtzite-type $\alpha\text{-GaN}$ determined by Raman spectroscopy. *Phys. Rev. B* **94**, 195201 (2016).
52. Larciprete, M. C. et al. Second order nonlinear optical properties of zinc oxide films deposited by low temperature dual ion beam sputtering. *J. Appl. Phys.* **97**, 023501 (2005).
53. Fan, Y. X., Eckardt, R. C., Byer, R. L., Chen, C. & Jiang, A. D. Barium borate optical parametric oscillator. *IEEE J. Quantum Electron.* **25**, 1196–1199 (1989).
54. Chen, C. et al. New nonlinear-optical crystal: LiB_3O_5 . *J. Opt. Soc. Am. B* **6**, 616–621 (1989).
55. Alford, W. J. & Smith, A. V. Wavelength variation of the second-order nonlinear coefficients of KNbO_3 , KTiOPO_4 , KTiOAsO_4 , LiNbO_3 , LiIO_3 , $\beta\text{-BaB}_2\text{O}_4$, KH_2PO_4 , and LiB_3O_5 crystals: a test of miller wavelength scaling. *J. Opt. Soc. Am. B* **18**, 524–533 (2001).
56. Adachi, S. Optical dispersion relations for GaP, GaAs, GaSb, InP, InAs, InSb, $\text{Al}_x\text{Ga}_{1-x}\text{As}$, and $\text{In}_{1-x}\text{Ga}_x\text{As}_y\text{P}_{1-y}$. *J. Appl. Phys.* **66**, 6030–6040 (1989).
57. Constable, E. & Lewis, R. A. Optical parameters of ZnTe determined using continuous-wave terahertz radiation. *J. Appl. Phys.* **112**, 063104 (2012).
58. Barker, A. S. & Ilegems, M. Infrared lattice vibrations and free-electron dispersion in GaN. *Phys. Rev. B* **7**, 743–750 (1973).
59. Ashkenov, N. et al. Infrared dielectric functions and phonon modes of high-quality ZnO films. *J. Appl. Phys.* **93**, 126–133 (2003).
60. Barker, A. S. & Loudon, R. Dielectric properties and optical phonons in LiNbO_3 . *Phys. Rev.* **158**, 433–445 (1967).
61. Liu, J., Guo, X., Dai, J. & Zhang, X.-C. Optical property of beta barium borate in terahertz region. *Appl. Phys. Lett.* **93**, 171102 (2008).
62. Xiong, G., Lan, G., Wang, H. & Huang, C. Infrared reflectance and raman spectra of lithium triborate single crystal. *J. Raman Spectrosc.* **24**, 785–789 (1993).
63. Rybak, A., Antsygin, V., Mamrashev, A. & Nikolaev, N. Terahertz optical properties of KTiOPO_4 crystal in the (-192)-150 °C temperature range. *Crystals* **11**, 125 (2021).
64. Fontana, M. D., Metrat, G., Servoin, J. L. & Gervais, F. Infrared spectroscopy in KNbO_3 through the successive ferroelectric phase transitions. *J. Phys. C* **17**, 483 (1984).
65. García de Abajo, F. J. & Howie, A. Retarded field calculation of electron energy loss in inhomogeneous dielectrics. *Phys. Rev. B* **65**, 115418 (2002).
66. Timbrell, D., You, J. ianW. ei, Kivshar, Y. S. & Panoiu, N. C. A comparative analysis of surface and bulk contributions to second-harmonic generation in centrosymmetric nanoparticles. *Sci. Rep.* **8**, 3586 (2018).
67. Krause, D., Teplin, C. W. & Rogers, C. T. Optical surface second harmonic measurements of isotropic thin-film metals: gold, silver, copper, aluminum, and tantalum. *J. Appl. Phys.* **96**, 3626–3634 (2004).
68. Weis, R. S. & Gaylord, T. K. Lithium niobate: summary of physical properties and crystal structure. *Appl. Phys. A-Mater. Sci. Process.* **37**, 191–203 (1985).
69. Anthur, A. P. et al. Continuous wave second harmonic generation enabled by quasi-bound-states in the continuum on gallium phosphide metasurfaces. *Nano Lett.* **20**, 8745–8751 (2020).
70. Guo, X., Zou, C. hang-L. ing & Tang, H. X. Second-harmonic generation in aluminum nitride microrings with 2500%/W conversion efficiency. *Optica* **3**, 1126–1131 (2016).
71. Caldwell, J. D. et al. Low-loss, infrared and terahertz nanophotonics using surface phonon polaritons. *Nanophotonics* **4**, 44–68 (2015).
72. Dai, S. et al. Tunable phonon polaritons in atomically thin van der Waals crystals of boron nitride. *Science* **343**, 1125–1129 (2014).

73. Naik, G. V., ShalaeV, V. M. & Boltasseva, A. Alternative plasmonic materials: beyond gold and silver. *Adv. Mater.* **25**, 3264–3294 (2013).
74. Simsek, E. Full analytical model for obtaining surface plasmon resonance modes of metal nanoparticle structures embedded in layered media. *Opt. Express* **18**, 1722–1733 (2010).
75. Law, S., Adams, D. C., Taylor, A. M. & Wasserman, D. Mid-infrared designer metals. *Opt. Express* **20**, 12155–12165 (2012).
76. Wu, Y. et al. Singular and nonsingular transitions in the infrared plasmons of nearly touching nanocube dimers. *ACS Nano* **18**, 15130–15138 (2024).
77. Johnson, P. B. & Christy, R. W. Optical constants of the noble metals. *Phys. Rev. B* **6**, 4370–4379 (1972).
78. Walther, M., Fischer, B., Schall, M., Helm, H. & Jepsen, P. U. Far-infrared vibrational spectra of all-trans, 9-cis and 13-cis retinal measured by THz time-domain spectroscopy. *Chem. Phys. Lett.* **332**, 389–395 (2000).
79. Maytorena, J. esúsA., Mochán, W. L. & Mendoza, B. S. Hydrodynamic model for sum and difference frequency generation at metal surfaces. *Phys. Rev. B* **57**, 2580–2585 (1998).

Acknowledgements

This work was supported by the European Research Council (Adv. Grant 101141220-QUEFES), the European Commission (FET-Proactive 101017720-eBEAM), the Spanish MICIU (PID2024-157421NB-I00 and Severo Ochoa CEX2024-001490-S), and the CERCA program.

Author contributions

F.J.G.A. conceived the concept. L.P. carried out the numerical calculations with input from all authors. All authors contributed to the analysis of the results and writing of the paper.

Competing interests

The authors declare no competing interests.

Additional information

Supplementary information The online version contains supplementary material available at <https://doi.org/10.1038/s41467-025-67288-1>.

Correspondence and requests for materials should be addressed to F. Javier García de Abajo.

Peer review information *Nature Communications* thanks Deng Pan and the other, anonymous, reviewer(s) for their contribution to the peer review of this work. A peer review file is available.

Reprints and permissions information is available at <http://www.nature.com/reprints>

Publisher's note Springer Nature remains neutral with regard to jurisdictional claims in published maps and institutional affiliations.

Open Access This article is licensed under a Creative Commons Attribution-NonCommercial-NoDerivatives 4.0 International License, which permits any non-commercial use, sharing, distribution and reproduction in any medium or format, as long as you give appropriate credit to the original author(s) and the source, provide a link to the Creative Commons licence, and indicate if you modified the licensed material. You do not have permission under this licence to share adapted material derived from this article or parts of it. The images or other third party material in this article are included in the article's Creative Commons licence, unless indicated otherwise in a credit line to the material. If material is not included in the article's Creative Commons licence and your intended use is not permitted by statutory regulation or exceeds the permitted use, you will need to obtain permission directly from the copyright holder. To view a copy of this licence, visit <http://creativecommons.org/licenses/by-nc-nd/4.0/>.

© The Author(s) 2025